PHYSICAL REVIEW B **90**, 020504(R) (2014)

Dirac fermions and superconductivity in the homologous structures $(Ag_xPb_{1-x}Se)_5(Bi_2Se_3)_{3m}$ $(m = 1,2)$

L. Fang,[1,*] C. C. Stoumpos,[2] Y. Jia,[3] A. Glatz,[2,4] D. Y. Chung,[2] H. Claus,[2] U. Welp,[2] W.-K. Kwok,[2] and M. G. Kanatzidis[1,2,†]

[1]*Department of Chemistry, Northwestern University, Evanston, Illinois 60208, USA*

[2]*Materials Science Division, Argonne National Laboratory, Argonne, Illinois 60439, USA*

[3]*Department of Physics and Astronomy, Northwestern University, Evanston, Illinois 60208, USA*

[4]*Department of Physics, Northern Illinois University, DeKalb, Illinois 60115, USA*

(Received 30 April 2014; published 9 July 2014)

A newly discovered topological insulator (TI) $(Ag_xPb_{1-x}Se)_5(Bi_2Se_3)_{3m}$ $(m = 2)$ has a band gap of 0.5 eV, the largest value reported in topological insulators. We present a magnetotransport study of the Dirac electrons of this compound in the quantum diffusion regime. Two-dimensional weak antilocalization due to the destructive interference of the Dirac electrons was observed. The phase coherence length of the Dirac electrons is independent of doping and disorder levels. This provides an indication of the backscattering immunity under the protection of time reversal invariance of the TI. We further report that the homologous compound $(Ag_xPb_{1-x}Se)_5(Bi_2Se_3)_{3m}$ $(m = 1)$ is a superconductor with a transition temperature $T_C = 1.7$ K. The related structures of these two phases allow lateral intergrowth of crystals to occur naturally, offering a potential platform to observe the Majorana fermion state at the boundary of two intergrown crystals.

DOI: 10.1103/PhysRevB.90.020504 PACS number(s): 73.20.At, 74.10.+v

The observation of novel quantum phenomena in topological insulators (TIs) is closely related to the discovery of new materials [1–4]. Numerous advances on TIs [5–10], both theoretical and experimental, were based on two binary bismuth compounds, Bi_2Se_3 and Bi_2Te_3. Material tailoring of Bi_2Se_3 with other structures can produce new phases that host topological states [11–14]. One example is the homologous series of layered structures of $(PbSe)_5(Bi_2Se_3)_{3m}$ $(m = 1,2)$ [15], and the presence of a Dirac cone in the $m = 2$ phase coupled with a large band gap of 0.5 eV [16]. Knowledge about this material, however, is very limited. Here we report on magnetotransport measurements of single crystal $m = 1$ and $m = 2$ phases. The latter exhibits two-dimensional (2D) weak antilocalization (WAL) due to the destructive interference of the Dirac electrons. The phase coherence length of the Dirac electrons is independent of doping and disorder levels, indicating the backscatter immunity of the TI $m = 2$ phase. Moreover, the $m = 1$ phase is a superconductor with a critical transition temperature of $T_C = 1.7$ K. The homologous structures of these two phases allow intergrowth of crystals to occur naturally. We thus propose a possibility to observe the Majorana fermion state at the boundary of two intergrown crystals.

The self-flux method was applied for single crystal synthesis. Nominal compositions of the starting materials are $Ag_xPb_5Bi_6Se_{14}$ and $Ag_xPbBi_4Se_7$ for the $m = 1$ and $m = 2$ phases, respectively. Intergrowth of the $m = 1$ and $m = 2$ phases was generally observed for crystals with sizes of larger than half a millimeter. However, phase-pure crystals with in-plane dimensions of 300–400 μm^2 can be separated from the ingot. Single crystal diffraction was carried out on a STOE Imaging Plate Diffraction Systems (IPDS) II diffractometer. Structure solution and refinement was conducted using the SHELX-97. Magnetization measurements were carried out using a homemade low-field (0.1 G) superconducting quantum interference device (SQUID) magnetometer operating at temperatures down to 1.2 K. Single crystals with thicknesses 7–40 μm were cut into rectangular shapes for both in-plane and c-axis transport characterization. The in-plane characterization adopts the standard four probe method with contacts featuring a Hall bar geometry. As for the c-axis measurements, two separated contacts were painted on both sides of a crystal. The current contacts spread over a large area of the cleaved surface to keep a uniform current flow in the normal direction. The voltage contacts were strictly aligned to avoid in-plane conduction. Transport measurements were conducted in a liquid ^{4}He variable temperature cryostat equipped with a triple-axis vector magnet system (AMI) for accurate field orientations. Superconducting transitions were measured in a liquid ^{3}He cryostat.

The structures of $(PbSe)_5(Bi_2Se_3)_{3m}$ $(m = 1,2)$ are stacks of layers of two building blocks [PbSe] and $[Bi_2Se_3]$, as shown in Figs. 1(b) and 1(c). The value of m designates the number of $[Bi_2Se_3]$ sheets that are sandwiched by consecutive [PbSe] slabs. The $[Bi_2Se_3]$ sheet is hexagonal and is the same as a quintuple layer (QL) of TI Bi_2Se_3. The [PbSe] sheet has tetragonal symmetry and is a two-atom-thick slice from the face-centered-cubic (fcc) structured PbSe. The lattice mismatch between $[Bi_2Se_3]$ and [PbSe] produces a stress that strongly distorts the slab of [PbSe] along the c axis for both homologous phases. The $m = 1$ phase features a large number of chemical bonds with a length of 3.25 Å between the [PbSe] and $[Bi_2Se_3]$ sheets creating a three-dimensional (3D) structure. In the $m = 2$ phase, the two adjacent QLs II and III are connected by van der Waals bonding [see Fig. 1(c)]. This weak bonding relaxes the stress and preserves the uniformity of the $[Bi_2Se_3]$ sheets. Crystal cleaving always occurs along the van der Waals plane and exposes an ideal surface of Bi_2Se_3 with Dirac fermions residing on it. By contrast, the $m = 1$ phase appears not to be a TI phase. As a matter of fact, angle

*lei.fang@northwestern.edu

†m-kanatzidis@northwestern.edu

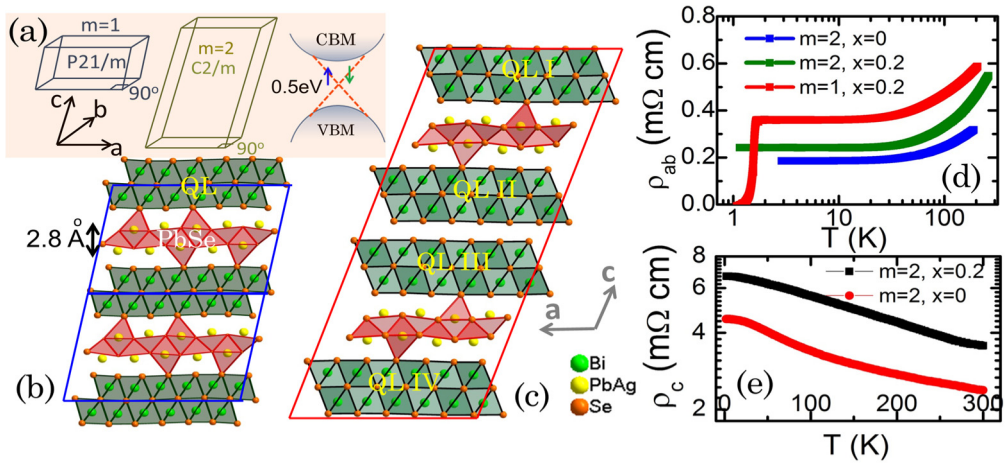

FIG. 1. (Color online) (a) Schematic pictures of the crystal symmetry of $(PbSe)_5(Bi_2Se_3)_{3m}$ ($m = 1,2$) and of a Dirac cone in the band structure of the $m = 2$ phase. (b) Structure of two unit cells of the $m = 1$ phase. The thickness of [PbSe] is ~2.8 Å. [PbSe] and $[Bi_2Se_3]$ are connected by chemical bonds. (c) Structure of one unit cell of the $m = 2$ phase. Bonds between QL-II and QL-III are of van der Waals type. Silver can replace Pb ions in the [PbSe] slabs. (d) Temperature dependent ρ_{ab} of $(Ag_xPb_{1-x}Se)_5(Bi_2Se_3)_6$ ($x = 0,0.2$) and $(Ag_{0.2}Pb_{0.8}Se)_5(Bi_2Se_3)_3$. (e) Temperature dependent ρ_c of the $m = 2$ phase. The resistivity anisotropies $\Gamma = \rho_c/\rho_{ab}$ at 2 K are 25(±3) and 28(±3) for doping $x = 0$ and 0.2, respectively.

resolved photoemission spectroscopy (ARPES) measurements observed a Dirac cone in $(PbSe)_5(Bi_2Se_3)_6$, in contrast to a regular band structure for $(PbSe)_5(Bi_2Se_3)_3$ [16]. To explain the different electronic structures, a scenario of topological phase transition has been proposed [16]. Here we further show that transition metals such as silver can replace in part Pb atoms in the structure up to levels of 25% while maintaining the TI character in $m = 2$ and inducing superconductivity in the $m = 1$ phase.

Our single crystal x-ray diffraction analysis detected unusually weak thermal displacement factors at the Se sites, suggesting Se vacancies in the $m = 2$ phase (see the Supplemental Material [17]). These vacancies donate electrons and elevate the Fermi level (E_F) toward the bottom of the conduction band. Both the temperature dependent resistivity of $(PbSe)_5(Bi_2Se_3)_6$ and Ag-doped $(Ag_{0.2}Pb_{0.8}Se)_5(Bi_2Se_3)_6$ exhibit semimetal behavior and moderately high residual resistivity [Fig. 1(d)]. The Hall resistances of the $m = 2$ phases exhibit nonlinear field dependence [Fig. 2(a)], suggesting that multiple types of carriers contribute to the transport processes, which, in our case, are the Dirac fermions on the surface and conventional electrons in the bulk. The carrier concentrations (n) of the two groups of electrons in a multiband system cannot be directly resolved by magnetotransport [18]. Approximately, the effective n of the bulk band is estimated using $R_{xy}(B = 2\ \mathrm{T})$ as $1.5–2 \times 10^{20}/\mathrm{cm}^3$ for the $m = 2$ phase. Silver doping donates holes and reduces the n to $5–7 \times 10^{19}/\mathrm{cm}^3$ for $(Ag_{0.2}Pb_{0.8}Se)_5(Bi_2Se_3)_6$.

Magnetoresistance (MR) measurements were conducted on bulk crystals of the $m = 2$ phase in tilted magnetic fields. As shown in Fig. 2(b), MR values for different tilted fields feature a cusp-shape curvature, a hallmark of WAL [19]. In the quantum diffusion regime, electrons can be localized due to the phase interference between a closed Feynman path and its time-reversal path. In TIs [20–23], both the π-Berry's phase of the Dirac electrons and the strong spin-orbit coupling (SOC) can destroy the phase interference and result in WAL. In addition to the WAL, the $m = 2$ phase exhibits weak anisotropy (Γ). The MR (at $\theta = 0°$, $\mu_0 H = 0.4$ T) is twice that of the MR (at $\theta = 90°$, $\mu_0 H = 0.4$ T), leading to $\Gamma \approx 2$. θ is the angle between the field and the c axis. The weakly anisotropic MR is consistent with the resistivity anisotropy

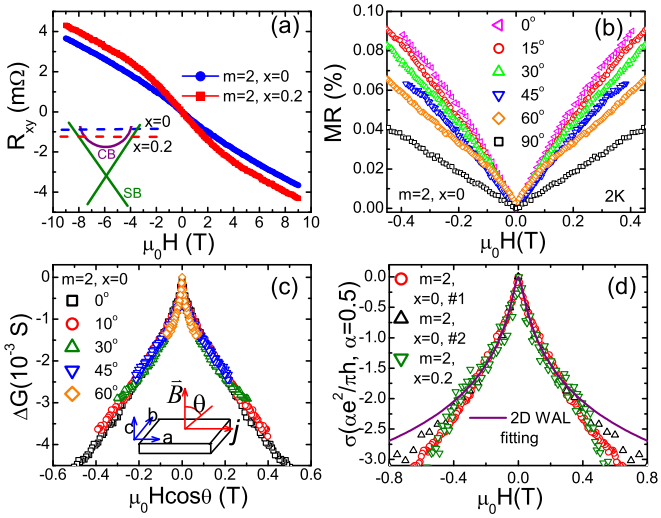

FIG. 2. (Color online) (a) Hall coefficient measurements of the $m = 2$ phase at 2 K exhibit a nonlinear field dependence. The inset schematically shows the coexistence of surface (SB) and bulk bands (CB). (b) MR measurement of bulk crystal $(PbSe)_5(Bi_2Se_3)_6$ at 2 K in tilted magnetic fields. (c) 2D scaling of the magnetoconductance of crystal $(PbSe)_5(Bi_2Se_3)_6$. The inset is a schematic picture of our angle dependent magnetoconductance measurements. (d) The scaled ΔG of two crystals (No. 1, No. 2) of $(PbSe)_5(Bi_2Se_3)_6$ and of a silver-doped crystal ($m = 2$, $x = 0.2$), in magnetic fields along the c axis. The solid curve is a fitting using the HLN equation.

$\rho_c/\rho_{ab} \simeq 28$. To unify, we define that the anisotropy of the $m = 2$ phase is moderate. Our determination agrees with the 3D classification of the $m = 2$ phase in the review article [4].

The WAL induced magnetoconductance (G) near zero field can be experimentally obtained from $\Delta G(B) = 1/R(B) - 1/R(0)$, and its angular dependence can be obtained from $\Delta G(B,\theta) = 1/R(B,\theta) - 1/R(B,90^\circ)$ [22]. $R(B,90^\circ)$ is the resistance when the field is parallel to the in-plane current. Figure 2(c) depicts the field dependent magnetoconductance of a bulk crystal $(PbSe)_5(Bi_2Se_3)_6$ at 2 K in various magnetic field directions. The magnetoconductance measured at various angles collapses onto one single curve when using the normal component of the applied field as the x coordinate. This scaling unveils the two-dimensional (2D) character of the WAL. 2D WAL was also observed in the silver-doped $m = 2$ phase (see the Supplemental Material [17]). The 2D magnetoconductance is not likely to arise from the moderately anisotropic bulk. Given the TI nature of the $m = 2$ phase, we associate the 2D WAL with the topological surface states. It is noticed that the absolute values of G in Fig. 2(c) is 50 times greater than the conductance quantum $2e^2/h$, pointing out multiple surface channels in our samples. These unexpected surface channels may be an indication of the proposed interface topological states [16]. However, defects such as the microscopic cracks in layered bulk crystals can also locally produce surface states and lead to this phenomenon as well. These multiple surface conducting channels tend to amplify the signal of one topological surface state and manifest their conducting weight in the total conductance despite the presence of a large amount of bulk electrons.

In order to more qualitatively understand the 2D WAL, the conductance of two crystals of the $m = 2$ phase and one doped specimen ($m = 2, x = 0.2$) were scaled to conductance quantum. Here, we assume that the 2D conducting channels in one crystal are identical and each channel carries one conductance quantum. The distinction between the top and bottom surface states of a TI thin film [21], possibly due to the substrate effect, is not included in our discussion. As shown in Fig. 2(d), it is striking that the WAL of different samples and doping levels can be scaled onto one curve over a field range from -0.4 to 0.4 T, indicating that a robust transport mechanism governs the $m = 2$ phase. The curvature of WAL is described by the phase coherence length [19] $l_\varphi = \sqrt{D\tau_\varphi}$, where the diffusion constant $D = \frac{1}{d}{v_F}^2\tau_e$, d is dimension, v_F denotes the Fermi velocity, τ_e is elastic scattering time, and τ_φ represents dephasing time. This scaling unveils that the l_φ are virtually independent of the specifics of the sample. To obtain a constant value of l_φ, both D and τ_φ have to be invariant. This observation can only be understood in the context of topological insulators. Since the Dirac dispersion relation is linear, $E(k) \sim k$, v_F of the Dirac electrons is independent of E_F and the doping level. τ_e is retained because backscattering is forbidden due to time reversal invariance [22,24,25]. τ_φ is not drastically altered unless magnetic impurities are present. Our experiments hence provide an indication of backscattering immunity in TI $(PbSe)_5(Bi_2Se_3)_6$ and Ag-doped samples.

The solid curve in Fig. 2(d) is a 2D fitting using the Hikami-Larkin-Nagaoka (HLN) theory [26]. Assuming that the inelastic scattering time is much longer than both spin-orbit and elastic scattering time, the equation of the WAL can be written as

$$\Delta\sigma(B) \cong -\alpha\frac{e^2}{\pi h}\left[\Psi\left(\frac{1}{2}+\frac{B_\varphi}{B}\right) - \ln\left(\frac{B_\varphi}{B}\right)\right], \quad (1)$$

where $\alpha = 1/2$. $\Psi(z)$ is the digamma function. $B_\varphi = \hbar/4el_\varphi{}^2$ is the characteristic field. $\hbar$ is the reduced Planck constant. The obtained B_φ is about 0.007 T and $l_\varphi \approx 160$ nm, comparable to the reported value of 310 nm in TI Bi_2Te_3 [22]. The 2D fitting, together with the observation of 2D magnetoconductance, the signature of backscattering immunity, and nonlinear Hall resistance, are fully consistent with the topological surface state of the material $(Ag_xPb_{1-x}Se)_5(Bi_2Se_3)_{3m}$ ($m = 2$). Other scenarios such as a trivial surface band [27] could lead to the 2D WAL in the presence of strong SOC. However, our magnetoconductance measurements on the $m = 1$ phase only demonstrate a standard 3D bulk WAL (see the Supplemental Material [17]), indicating a weak influence of this effect. Given the analogous surface condition of the $m = 1$ and $m = 2$ phases, the trivial surface band is likely less essential in the TI $m = 2$ phase as well.

We were not able to induce superconductivity in $(PbSe)_5(Bi_2Se_3)_6$ by doping with silver and other transition metals (see the Supplemental Material [17]). However, we found that the Ag-doped $m = 1$ phase $(Ag_xPb_{1-x}Se)_5(Bi_2Se_3)_3$ is superconducting. As shown in Fig. 3(a), the resistance of $(Ag_{0.2}Pb_{0.8}Se)_5(Bi_2Se_3)_3$ starts to drop at 1.6 K and zero resistance is reached at 0.55 K. Superconductivity was observed for different doping levels. Figure 3(b) presents the magnetization measurements of $(Ag_xPb_{1-x}Se)_5(Bi_2Se_3)_3$ ($x = 0.1$–0.25). At doping levels $x < 0.1$, the diamagnetic signal is extremely weak. At doping

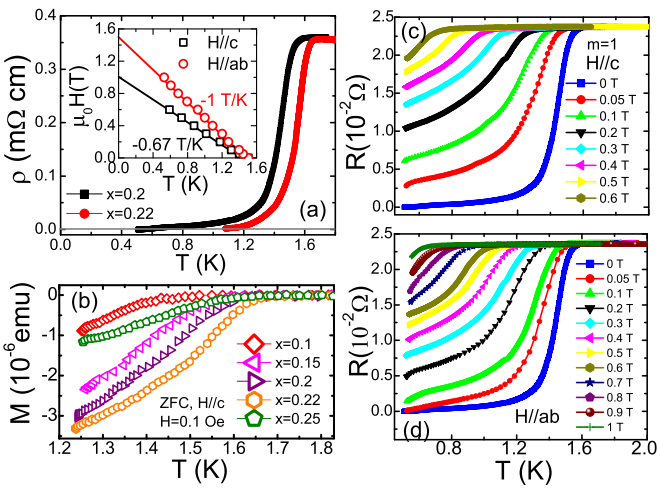

FIG. 3. (Color online) (a) Temperature dependent resistivity of $(Ag_xPb_{1-x}Se)_5(Bi_2Se_3)_3$ ($x = 0.2, 0.22$). Both samples show superconducting transitions below 1.6 K and zero resistances. The inset is a H_{C2} plot for doping $x = 0.2$ with fields applied in plane and out of plane. The straight solid lines are guides to the eye. (b) Temperature dependent magnetization of crystals $(Ag_xPb_{1-x}Se)_5(Bi_2Se_3)_3$ ($x =$ 0.1–0.25). T_C varies with the silver doping. ZFC means zero-field cooling. (c) and (d) are temperature dependent resistances of the superconducting sample in fields applied along out of plane and in plane.

of $x > 0.25$, the structure of $(Ag_xPb_{1-x}Se)_5(Bi_2Se_3)_3$ becomes unstable. The highest T_C is 1.7 K. In order to determine the upper critical fields (H_{C2}) and superconducting anisotropy (γ), we suppressed the superconductivity by applying magnetic fields in plane and out of plane, as shown in Figs. 3(c) and 3(d). Using 90% of the normal-state resistance as a criterion, we mapped out the superconducting phase diagram of $(Ag_{0.2}Pb_{0.8}Se)_5(Bi_2Se_3)_3$, shown in the inset of Fig. 3(a). At $T \leqslant T_C$, $\frac{dH_{C2}^c}{dT} \approx -0.67$ T/K and $\frac{dH_{C2}^{ab}}{dT} \approx -1$ T/K. Using the Werthamer-Helfand-Hohenberg formula [28] $H_{C2}(0) = -0.693 T_C (dH_{C2}/dT)_{T=T_c}$, the zero temperature upper critical fields are $H_{C2}^c \approx 0.74$ T and $H_{C2}^{ab} \approx 1.1$ T. The Ginzburg-Landau in-plane coherence length can be obtained from $\xi_0^{GL} = \sqrt{\phi_0/2\pi H_{C2}^c} = 21.7$ nm, where ϕ_0 is the flux quantum. The superconducting anisotropy [29] is written as $\gamma = \sqrt{\frac{m_c}{m_{ab}}} = \frac{\xi_{ab}}{\xi_c} = \frac{H_{C2}^{ab}}{H_{C2}^c} = 1.5$, where $\frac{m_c}{m_{ab}}$ is the ratio of effective mass matrix elements. The near-isotropic characteristics of H_{C2} are consistent with our structure determination. In addition to the charge doping effect, lattice strain [30,31] could be another driven force for the superconductivity in the $m = 1$ phase. Lattice shrinkage along the c axis was resolved when 20% Pb was substituted with Ag.

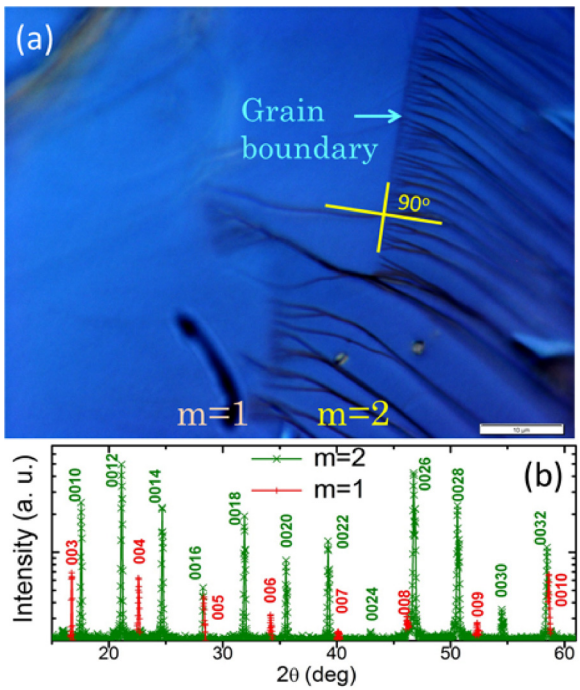

FIG. 4. (Color online) (a) Optical image of a cleaved superconducting crystal. Grain boundaries divide the crystal in two parts. The right part exhibits a more cleavable characteristic than the part on the left. This distinct topography indicates the different structures of these two domains. The domain angles, as shown as the yellow cross, are ~90°, consistent with the solved crystallographic data of $(PbSe)_5(Bi_2Se_3)_{3m}$ ($m = 1,2$). The right domain is ascribed to the $m = 2$ phase and the left part is the $m = 1$ phase. (b) X-ray diffraction of a superconducting crystal along the c axis. The two sets of (00l) peaks unveil that two phases intergrow in the ab plane, consisting well with the image in (a).

The superconducting $(Ag_xPb_{1-x}Se)_5(Bi_2Se_3)_3$ and the TI character of $(Ag_xPb_{1-x}Se)_5(Bi_2Se_3)_6$ may provide an opportunity to detect Majorana fermions at the interface of these two phases [32]. Because of the very close matching of in-plane lattice parameters (see the Appendix), the $(Ag_xPb_{1-x}Se)_5(Bi_2Se_3)_3$ crystals can be easily intergrown with crystals of $(Ag_xPb_{1-x}Se)_5(Bi_2Se_3)_6$ with limited strain. This creates a natural interface between a superconductor and a topological insulator. Taking advantage of the proximity effect, superconductivity can transform some of the Dirac fermions of the topological state into an Andreev surface state [32]. Hence, Majorana fermions could be observable at the boundary of the $(Ag_{0.2}Pb_{0.8}Se)_5(Bi_2Se_3)_3$ and the $(Ag_{0.2}Pb_{0.8}Se)_5(Bi_2Se_3)_6$ domains. The interface of the intergrown samples was imaged with polarized light on a cleaved surface of a superconducting crystal. As shown in Fig. 4(a), two domains with distinct cleavage morphologies were observed to grow together. The domain boundary is uniform and may allow local detection techniques.

In conclusion, 2D WAL behaviors exist in TI $(Ag_xPb_{1-x}Se)_5(Bi_2Se_3)_6$. A scaling law of the WAL for different doping and impurity levels indicates the backscattering immunity of this TI. We further report that the homologous compound $(Ag_xPb_{1-x}Se)_5(Bi_2Se_3)_3$ is a superconductor with a transition temperature $T_C = 1.7$ K. The related structures of these two phases allow lateral intergrowth of crystals to occur naturally, offering a potential platform to observe the Majorana fermion state at the boundary of two intergrown crystals.

We are grateful to L. Bouchard and Kang L. Wang for useful discussions. This research was supported by the Defense Advanced Research Project Agency (DARPA), Award No. N66001-12-1-4034. Transport and magnetization measurements were supported by the Department of Energy, Office of Basic Energy Sciences, under Contract No. DE-AC02-06CH11357 (D.Y., C.C.S., Y.J., H.C., A.G., U.W., W.K.K.).

APPENDIX

Crystal data: (1) $(PbSe)_5(Bi_2Se_3)_6$, monoclinic, space group $C2/m$, $c = 52.918(10)$ Å, $\gamma = 90.00°$, $b = 4.1774(8)$ Å, $\beta = 107.224(3)°$, $a = 21.551(4)$ Å, $\alpha = 90.00°$, $T = 293$ K, $V = 4550.4(15)$ Å^3, $Z = 4$, reflections collected 26 308, independent reflections 6220 [$R_{int} = 0.0971$], completeness to $\theta = 29.00°$, 90.8%, refinement method, full-matrix least squares on F^2, goodness of fit, 1.054, final R indices [$>2\sigma$(I)] $R_{obs} = 0.0708$, $wR_{obs} = 0.1950$, R indices [all data] $R_{all} = 0.1321$, $wR_{all} = 0.2208$.

(2) $(Ag_{0.2}Pb_{0.8}Se)_5(Bi_2Se_3)_6$, monoclinic, space group $C2/m$, $c = 52.927(4)$ Å, $\gamma = 90.00°$, $b = 4.1747(2)$ Å, $\beta = 107.423(6)°$, $a = 21.5211(17)$ Å, $\alpha = 90.00°$, $T = 293$ K, $V = 4537.0(5)$ Å^3, $Z = 4$, reflections collected 22 210, independent reflections 6894 [$R_{int} = 0.1299$], completeness to $\theta = 29.00°$, 99.3%, refinement method, full-matrix least squares on F^2, goodness of fit, 0.915, final R indices [$>2\sigma$(I)] $R_{obs} = 0.0589$, $wR_{obs} = 0.0810$, R indices [all data] $R_{all} = 0.1504$, $wR_{all} = 0.1042$.

(3) $(PbSe)_5(Bi_2Se_3)_3$, monoclinic, space group $P21/m$, $c = 15.9840(12)$ Å, $\gamma = 90.00°$, $b = 4.1915(3)$ Å,

$\beta = 97.4750(10)^\circ$, $a = 21.4727(16)$ Å, $\alpha = 90.00^\circ$, $T = 293$ K, $V = 1426.38(18)$ Å^3, $Z = 2$, reflections collected 7977, independent reflections 3359 [$R_{\rm int} = 0.1129$], completeness to $\theta = 29.00^\circ$, 93.1%, refinement method, full-matrix least squares on F^2, goodness of fit, 0.859, final R indices [$>2\sigma$(I)] $R_{\rm obs} = 0.0624$, $wR_{\rm obs} = 0.1389$, R indices [all data] $R_{\rm all} = 0.1091$, $wR_{\rm all} = 0.1536$. $R = \Sigma||F_o| - |F_c||/\Sigma|F_o|$, $wR = \{\sum[w(|F_o|^2 - |F_c|^2)^2]/\sum[w(|F_o|^4)]\}^{1/2}$, and calc $w = 1/[\sigma^2(F_o^2) + (0.0988P)^2 + 0.0000P]$, where $P = (F_o^2 + 2F_c^2)/3$.

[1] M. Z. Hasan and C. L. Kane, Rev. Mod. Phys. **82**, 3045 (2010).
[2] X.-L. Qi and S.-C. Zhang, Rev. Mod. Phys. **83**, 1057 (2011).
[3] J. E. Moore, Nature (London) **464**, 194 (2010).
[4] Y. Ando, J. Phys. Soc. Jpn. **82**, 102001 (2013).
[5] H. J. Zhang, C.-X. Liu, X.-L. Qi, X. Dai, Z. Fang, and S.-C. Zhang, Nat. Phys. **5**, 438 (2009).
[6] D. Hsieh *et al.*, Nature (London) **460**, 1101 (2009).
[7] D.-X. Qu, Y. S. Hor, J. Xiong, R. J. Cava, and N. P. Ong, Science **329**, 821 (2010).
[8] J. G. Analytis, R. D. McDonald, S. C. Riggs, J.-H. Chu, G. S. Boebinger, and I. R. Fisher, Nat. Phys. **6**, 960 (2010); J. G. Analytis, J.-H. Chu, Y. Chen, F. Corredor, R. D. McDonald, Z. X. Shen, and I. R. Fisher, Phys. Rev. B **81**, 205407 (2010).
[9] Y. Zhang *et al.*, Nat. Phys. **6**, 584 (2010).
[10] F. Xiu *et al.*, Nat. Nanotechnol. **6**, 216 (2011).
[11] R. J. Cava, H. W. Ji, M. K. Fuccillo, Q. D. Gibson, and Y. S. Hor, J. Mater. Chem. C **1**, 3176 (2013).
[12] Q. D. Gibson *et al.*, Phys. Rev. B **88**, 081108(R) (2013).
[13] Y. S. Hor, A. J. Williams, J. G. Checkelsky, P. Roushan, J. Seo, Q. Xu, H. W. Zandbergen, A. Yazdani, N. P. Ong, and R. J. Cava, Phys. Rev. Lett. **104**, 057001 (2010).
[14] S. V. Eremeev *et al.*, Nat. Commun. **3**, 635 (2012).
[15] M. G. Kanatzidis, Acc. Chem. Res. **38**, 359 (2005).
[16] K. Nakayama, K. Eto, Y. Tanaka, T. Sato, S. Souma, T. Takahashi, K. Segawa, and Y. Ando, Phys. Rev. Lett. **109**, 236804 (2012).
[17] See Supplemental Material at http://link.aps.org/supplemental/10.1103/PhysRevB.90.020504 for brief description of materials synthesis, structural details, transport characterization and doping effect.
[18] L. Fang, H. Luo, P. Cheng, Z. Wang, Y. Jia, G. Mu, B. Shen, I. I. Mazin, L. Shan, C. Ren, and H.-H. Wen, Phys. Rev. B **80**, 104508(R) (2009).
[19] G. Bergmann, Phys. Rep. **107**, 1 (1984).
[20] H. Peng, K. Lai, D. Kong, S. Meister, Y. L. Chen, X. L. Qi, S. C. Zhang, Z. X. Shen, and Y. Cui, Nat. Mater. **9**, 225 (2010).
[21] J. Chen *et al.*, Phys. Rev. Lett. **105**, 176602 (2010); J. Chen, X. Y. He, K. H. Wu, Z. Q. Ji, L. Lu, J. R. Shi, J. H. Smet, and Y. Q. Li, Phys. Rev. B **83**, 241304(R) (2011).
[22] H.-T. He, G. Wang, T. Zhang, I.-K. Sou, G. K. L. Wong, J.-N. Wang, H.-Z. Lu, S.-Q. Shen, and F.-C. Zhang, Phys. Rev. Lett. **106**, 166805 (2011).
[23] M. R. Lang *et al.*, Nano Lett. **13**, 48 (2013).
[24] T. Zhang *et al.*, Phys. Rev. Lett. **103**, 266803 (2009).
[25] P. Roushan, J. Seo, C. V. Parker, Y. S. Hor, D. Hsieh, D. Qian, A. Richardella, M. Z. Hasan, R. J. Cava, and A. Yazdani, Nature (London) **460**, 1106 (2009).
[26] S. Hikami, A. I. Larkin, and Y. Nagaoka, Prog. Theor. Phys. **63**, 707 (1980).
[27] S. LaShell, B. A. McDougall, and E. Jensen, Phys. Rev. Lett. **77**, 3419 (1996).
[28] N. R. Werthamer, E. Helfand, and P. C. Hohenberg, Phys. Rev. **147**, 295 (1966).
[29] W. E. Lawrence and S. Doniach, in *Proceedings of the 12th International Conference on Low Temperature Physics*, edited by E. Kanda (Keigaku, Tokyo, 1971), p. 361.
[30] S. R. Saha, N. P. Butch, K. Kirshenbaum, J. Paglione, and P. Y. Zavalij, Phys. Rev. Lett. **103**, 037005 (2009).
[31] J. Engelmann *et al.*, Nat. Commun. **4**, 2877 (2013).
[32] L. Fu and C. L. Kane, Phys. Rev. Lett. **100**, 096407 (2008).